Myeloid-to-mesenchymal NGF-p75 signaling coordinates skeletal cell migration during repair

Running Title: NGF-p75 signaling in bone repair

Jiajia Xu,[1]† Zhao Li,[1]† Robert J. Tower,[2]† Stefano Negri,[1,3] Yiyun Wang,[1] Carolyn A. Meyers,[1] Takashi Sono,[1] Qizhi Qin,[1] Amy Lu,[1] Edward F. McCarthy,[1] Thomas L. Clemens,[2,4] Aaron W. James,[1]*

[1]Department of Pathology, Johns Hopkins University, Baltimore, MD 21205

[2]Department of Orthopaedics, Johns Hopkins University, Baltimore, MD 21205

[3]Department of Orthopaedics and Traumatology, University of Verona, Verona 37129, Italy

[4]Baltimore Veterans Administration Medical Center, Baltimore, MD 21201.

† These authors contributed equally to this work.

*Corresponding Author:

Aaron W. James, M.D., Ph.D., 720 Rutland Avenue, Room 524A, Baltimore, MD 21205, Phone: (410) 502-4143, Email: awjames@jhmi.edu

Abstract

Tissue repair relies on the coordination of mesenchymal precursor cells (MPCs) which migrate into the injury site, along with the invasion of blood vessels and sensory nerves. Our prior observations found that the neurotrophin Nerve growth factor (NGF) regulates sensory nerve ingrowth to skeletal repair sites via its high-affinity receptor. A body of work in cancer biology suggest that neurotrophins also engage their low-affinity receptor p75 to mediate cellular migration. Here, we observed conditional deletion of *p75* in MPCs or osteoblasts to disrupt bone repair independent of neurovascular ingrowth. Single cell sequencing identified defects in migration and wound healing among MPC populations. Deletion of *Ngf* among myeloid cells phenocopied *p75* conditional deletion animals. *In vitro* studies confirmed a myeloid-to-mesenchymal NGF-p75 axis which operates to induce cellular migration. Together, our data suggest a direct effect of myeloid-derived NGF on progenitor cells, in parallel to sensory nerve recruitment, required for injury repair.

Introduction

The regeneration of craniofacial bones of the mammalian skeleton requires the action of both intrinsic and extrinsic inductive factors from multiple cell types. Unlike the appendicular skeleton, intramembranous cranial bones form and are healed without a cartilaginous template by condensations of mesenchymal progenitor cells (*1*). Recent studies from our laboratory have demonstrated an essential role for skeletal sensory nerves in healing of experimental injuries in adult mouse bone, including calvarial bones (*2, 3*). Nerve growth factor (NGF) via its high-affinity receptor tropomyosin receptor kinase A (TrkA) regulates skeletal re-innervation, which is essential for later elements of bone repair, including revascularization and bone matrix deposition (*2-4*). However, emerging evidence suggests that neurotrophin signaling may have more pleiotropic effects in bone repair than previously considered.

In addition to induction of nerve ingrowth and promotion of nerve survival, pro-NGF binds to its low-affinity receptor p75 (encoded by *Ngfr*), which is present in a variety of mesenchymal cells (*5*). p75 expression has been correlated to cell migration and invasion in the fields of developmental and cancer biology. For example, Schwann cell migration from the dorsal root ganglia is significantly impaired in p75 null embryos (*6*). Likewise, p75-dependent signaling has an essential role in the migration of epidermal Langerhans cells (*7*). Similar observations have been made in neoplastic cells, in which stable knockdown of p75 in melanoma cells reduced cell migration and expression of major regulatory gene networks for cell migration (*8, 9*). NGF binding to the p75 receptor stimulates migration and initiates recruitment of various adaptors, which activate nuclear factor kappa B (NF-κB), Ras homolog family member a (RhoA), and c-Jun N-terminal kinase (JNK) signaling (*10, 11*).

56

57 In this study, we have identified an alternate role for NGF signaling in the bone reparative
58 process, one independent of skeletal sensory nerves. Depletion of *p75* in platelet-derived growth
59 factor receptor α (PDGFRα)$^{+}$ mesenchymal cells or osteocalcin (OC)$^{+}$ osteoblasts impaired
60 cellular migration into an osseous wound. Transcriptomics identified new mesenchymal
61 subpopulations with potential roles in cell migration and immune response, altered in the context
62 of *p75* deletion. Further, we identified an immune-to-skeletal cell signaling axis involving
63 myeloid/macrophage-derived NGF which acts to directly stimulate skeletal cell migration during
64 early bone repair.

65

66 **Results**

67 ***p75 is critical for stromal cell migration and calvarial regeneration***

68 *p75*-expressing cells in the uninjured skull and injured site were identified using a
69 previously validated PDGFRα-CreER^{T2};mT/mG (PDGFRα$^{mT/mG}$) reporter animal (*12*) (**Fig.**
70 **1A,B**). Lineage tracing of PDGFRα-expressing cells was based on tamoxifen (TM)
71 administration to promote the activity of inducible Cre, starting at 8 weeks of age. A circular
72 bone defect was created in the non-suture associated frontal bone 14 days after the last TM
73 administration. Within the frontal bone, p75 protein was detected at low levels in the
74 overlying periosteum and coincided with PDGFRα reporter activity in bone lining cells
75 (**Fig. 1B**). Following injury, a notable expansion of the p75^{+}Pdgfrα^{+} cell population was
76 detected along the outer edge of the injury defect site (**Fig. 1B**). To assess the requirement for
77 p75 in calvarial defect repair, *p75*$^{fl/fl}$ animals were crossed with PDGFRα$^{mT/mG}$ lines to yield
78 *p75*$^{fl/fl}$;PDGFRα$^{mT/mG}$ (*p75*^{PDGFRα}) animals. *p75*$^{fl/fl}$;mT/mG animals (*p75*$^{fl/fl}$) were used as

79 controls. Validation for *p75* deletion was performed using p75 immunohistochemistry on
80 calvarial injury sites within the *p75*$^{fl/fl}$ and *p75*$^{PDGFR\alpha}$ mice (**Fig. 1C**). p75 immunohistochemical
81 staining was significantly reduced in *p75*$^{PDGFR\alpha}$ defect sites, in comparison to *p75*$^{fl/fl}$ control
82 defects. Next, frontal bone healing was assessed following *p75* deletion in PDGFRα-expressing
83 cells over a 4-week period (**Fig. 1D-J**). Results demonstrated impaired bone healing among
84 *p75*$^{PDGFR\alpha}$ animals, relative to *p75*$^{fl/fl}$ controls. Micro-CT reconstructions and cross-sectional
85 images demonstrated impaired re-ossification among *p75*$^{PDGFR\alpha}$ mice (**Fig. 1D**). Quantitative
86 micro-CT metrics of bone healing were reduced among *p75*$^{PDGFR\alpha}$ mice, including Bone Volume
87 (BV, **Fig. 1E**, 68.3% reduction), fractional Bone Volume (BV/TV, **Fig. 1F**, 68.3% reduction),
88 mean diameter of the bone defect area (**Fig. 1G**, 40.9% increase), Bone fractional area (BFA,
89 **Fig. 1H**, 54.8% reduction), and bone healing score – a previously validated semi-quantitative 4
90 point scoring system (*13*) (**Fig. 1I**, 30.0% reduction in comparison to *p75*$^{fl/fl}$). H&E staining
91 confirmed a significant impairment of defect healing between bony fronts in *p75* mutant mice
92 (**Fig. 1J**, black arrowheads).
93
94 To determine potential mechanisms driving this impaired bone healing, Ki67 immunostaining
95 was first conducted to interrogate potential differences in proliferation (**Fig. 1K**). These results
96 failed to show any significant differences in cell expansion, suggesting the impaired healing
97 observed in *p75*$^{PDGFR\alpha}$ mice was not the result of reduced cell proliferation. Another potential
98 mechanism through which defect repair could be inhibited in p75 mutant mice is the failed
99 recruitment of regenerating mesenchymal cells to the defect site. To assess progenitor cell
100 migration into the defect, a lineage tracing strategy was employed using PDGFRα$^{mT/mG}$ animals.
101 PDGFRα reporter activity highlights stromal cells which are recruited to populate the bone injury

102 site. Deletion of *p75* in PDGFRα^{+} stromal progenitors resulted in a prominent decrease in
103 stromal cell migration into the central defect region (**Fig. 1L**). This impaired recruitment of
104 PDGFRα^{+} progenitors led to a reduced number of mature osteoblasts among *p75*^{PDGFRα} animals,
105 as assessed by immunohistochemical staining for Osteocalcin (**Fig. 1M**). Our previous reports
106 have demonstrated that specific impairment of the NGF-TrkA signaling axis leads to an impaired
107 invasion of both the vasculature and sensory nerves into the cranial defect region (*3*). To
108 determine whether a similar phenomenon may also be contributing to our impaired healing
109 deficiencies, vascularity and innervation within the defect site were next evaluated (**Fig. 1N,O**).
110 CD31 immunostaining of endothelium and TUBB3 immunostaining of axons suggested no
111 difference in defect site revascularization or re-innervation among *p75*$^{fl/fl}$ and *p75*^{PDGFRα} mice. In
112 aggregate, inhibition of p75 signaling in PDGFRα^{+} stromal cells led to significant reductions in
113 injury-associated cell migration and a significant delay in bone defect healing, independent of
114 changes in neurovasculature in bone.
115
116 ***Depletion of p75 in osteoblasts impairs osteoblast migration and calvarial healing***
117 To further delineate the cell stage-specific expression of p75, uninjured calvarial samples
118 were immunostained for p75 and the mature osteoblast marker OCN (**Fig. 2A**). These
119 studies confirmed that p75 is indeed also expressed in mature osteogenic cells lining the
120 periosteal bone surface. To assess the cell-specific requirements of *p75* in osteoblasts, *p75*$^{fl/fl}$
121 animals were crossed with the Osteocalcin-Cre line to yield *p75*$^{fl/fl}$; Osteocalcin-Cre (*p75*^{OC})
122 animals. *p75*^{OC} animals had normal size and weight (**Fig. S1A,B**). Validation for *p75* deletion
123 was next performed using p75 immunohistochemistry on calvarial injury sites within the *p75*$^{fl/fl}$
124 and *p75*^{OC} mice (**Fig. 2B,C**). Micro-CT analysis of uninjured frontal bones showed a slightly
125 decreased BV and increased bone mineral density among *p75*^{OC} animals (**Fig. S1C-G**). To

126 determine the role of osteoblast-specific p75 in injury repair, *p75*$^{fl/fl}$ and *p75*^{OC} mice were
127 analyzed 4 weeks after frontal bone defect creation (**Fig. 2D-I**). Micro-CT imaging demonstrated
128 a reduction in defect re-ossification among *p75*^{OC} animals **Fig. 2D**), confirmed by quantitative
129 micro-CT metrics of bone formation which demonstrated a significant reduction in all
130 parameters among *p75*^{OC} animals, including BV (**Fig. 2E**, 48.5% reduction), BV/TV (**Fig. 2F**,
131 48.5% reduction), an increase in remaining non-ossified diameter of the defect (**Fig. 2G**, 20.0%
132 increase), BFA (**Fig. 2H**, 35.7% reduction), and semi-quantitative bone healing score (**Fig. 2I**,
133 21.6% reduction in comparison to *p75*$^{fl/fl}$).
134
135 In a mechanism similar to our above reported *p75*$^{PDGFR\alpha}$ mice, deletion of *p75* in OCN^{+}
136 osteoblasts also led to a prominent decrease in progenitor cell migration into the defect site, as
137 assessed by flow cytometry for PDGFRα among CD31^{-}CD45^{-}Ter119^{-} cells (**Fig. 2J,K**).
138 Likewise, a similar 59.6% reduction in OCN^{+} osteoblasts was observed among *p75*^{OC} animals
139 (**Fig. 2L**). Similar to *p75*$^{PDGFR\alpha}$ mice, vascularization (**Fig. 2M**) and innervation (**Fig. 2N**) within
140 the defect site were unaffected in *p75*^{OC} mice. In sum, *p75* in OC-expressing osteoblasts is
141 essential for osseous repair.
142
143 ***Single cell transcriptomic profiling of total cells and mesenchymal lineage subpopulation***
144 To further understand the mechanisms driving impaired defect repair in p75-deficient mice, we
145 employed single-cell RNA sequencing (scRNA-seq) of cells derived from the defect site of
146 *p75*$^{fl/fl}$ and *p75*$^{PDGFR\alpha}$ mice at 7 days post-injury (**Fig. 3A**). Unsupervised clustering identified 8
147 groups (**Fig. 3B**), identified using expression patterns of known marker genes, including 2
148 groups of mesenchymal lineage cells (expressing *Paired related homeobox 1* (*Prrx1*)*, Platelet*

149 *derived growth factor receptor alpha* (*Pdfgra*)*, Msh homeobox 1* (*Msx1*)*, Twist family BHLH*
150 *transcription factor 1* (*Twist1*), and *Runt-related transcription factor 2* (*Runx2*)), 5 groups of
151 hematopoietic cells (expressing *Protein tyrosine phosphatase receptor type C* (*Ptprc*) encoding
152 CD45), and 1 group of endothelial cells/pericytes (expressing *Regulator of G-protein signaling 5*
153 (*Rgs5*)*,* and *Endomucin* (*Emcn*)) (**Fig. 3C**). While each cluster was represented by cells from
154 both $p75^{fl/fl}$ and $p75^{PDGFR\alpha}$ mice, some shifts in cluster proportions were observed, including
155 enrichment of mesenchymal cluster cells derived from $p75^{fl/fl}$ mice (**Fig. S2A,B**). Specificity of
156 Cre recombination was confirmed in sequenced data in which EGFP expression was restricted to
157 the PDGFRα-expressing mesenchymal clusters (**Fig. S2C**) and almost exclusively expressed in
158 $p75^{PDGFR\alpha}$-derived cells (**Fig. S2D**). Pathway analysis of differentially expressed genes (DEGs)
159 revealed GO term enrichment in cell adhesion, positive regulation of cell migration, osteoblast
160 differentiation, and wound healing in $p75^{fl/fl}$ mice (**Fig. 3D**). In contrast, immune system process,
161 inflammatory response, and regulation of cell shape were enriched in cells from $p75^{PDGFR\alpha}$ mice,
162 implying altered cell shape, differentiation and matrix interactions (**Fig. 3D**). Focused analysis of
163 mesenchymal lineage cells yielded 8 subpopulations (**Fig. 3E**). Early stem markers *Cd34*, *Thy1*
164 were predominantly expressed in cluster 1 and 2, while multi-lineage progenitor markers Actin
165 alpha 2, smooth muscle (*Acta2*) and Scleraxis (*Scx*) showed enriched expression in cluster 3/4
166 (**Fig. 3F**). Cluster 7 was classified as being likely derived from the dura mater owing to the
167 selective expression of *Forkhead box protein C2* (*Foxc2*), while cluster 8 cells was found to
168 express mature osteoblast markers *Bone gamma-carboxyglutamate protein 2* (*Bglap2*) and
169 *Secreted phosphoprotein 1* (*Spp1*) (**Fig. 3F**). Deletion of *p75* in mesenchymal cells was further
170 validated by downstream signaling-related gene expression, including genes of Rho, NF-κB and
171 mitogen-activated protein kinase (MAPK) signaling pathways (**Fig. S3**). Pathway analysis of the

172 total mesenchymal cell populations showed that osteogenesis-related signaling pathways were
173 inhibited among *p75*$^{PDGFR\alpha}$ cells, including Notch, Bone morphogenetic protein (BMP),
174 Transforming growth factor beta (TGFβ), Fibroblast growth factor (FGF), and Hippo signaling
175 (**Fig. 3G**). Interestingly, pathway analysis of cluster-specific DEGs showed specific enrichment
176 in GO terms such as cell adhesion, regulation of actin cytoskeleton organization, and cell
177 migration, in cluster 5 cells (**Fig. 3H**). Owing to our previous results suggesting an impaired
178 migration/recruitment of progenitor cells into the defect area, we further analyzed gene lists
179 linked to biological functions needed for cell migration (**Fig. 3I**). Consistent with our cluster
180 DEG assessment and in vivo results, cluster 5 showed significant enrichment for genes linked to
181 receptor-mediated extracellular matrix interaction and cytokine receptor-mediated signaling,
182 both of which were reduced in *p75*$^{PDGFR\alpha}$ cells (**Fig. 3I**). This data further suggested that p75
183 signaling within mesenchymal lineage cells is essential for cellular migration and osteogenic
184 differentiation during bone injury repair.
185
186 ***p75 signaling plays a critical role in cell migration and osteogenic differentiation in vitro***
187 To further determine the effect of p75 on stromal cell activity, primary neonatal mouse calvarial
188 cells (NMCCs) from *p75*$^{fl/fl}$ animals were isolated and treated with adenovirus encoding the Cre
189 recombinase (Ad-Cre) or control (Ad-GFP). The efficiency of *p75* deletion was confirmed by
190 qPCR (**Fig. 4A**) and validated by downstream signaling-related gene expression of RhoA, NF-κ
191 B and MAPK signaling pathways (**Fig. S4**). Consistent with our *in vivo* analysis, NMCCs
192 showed no change in cell proliferation rates among Ad-Cre- and Ad-GFP-treated groups (**Fig.
193 4B**). We did not observe an increase in apoptosis after Ad-Cre treatment by TUNEL assay (**Fig.**

194 **4C**). However, *p75* deletion reduced cell migration in wound-healing and transwell assays (**Fig.**
195 **4D,E**) as well as impaired osteogenic differentiation (**Fig. 4F,G**).
196
197 Next, the changes in the transcriptome of Ad-GFP- and Ad-Cre-treated NMCCs were examined
198 using bulk RNA sequencing (RNA-seq). 14,668 protein-coding genes were expressed across all
199 samples and had functional annotations. 577 transcripts, 3.93% of the total, showed a >2fold
200 change (FC) increase among Ad-Cre-treated cells (red dots; 381 transcripts showed a significant
201 increase ($p<0.05$)), while 399 transcripts, 2.72% of the total, showed a >2FC increase among Ad-
202 GFP-treated cells (green dots; 219 transcripts showed a significant decrease ($p<0.05$)) (**Fig. 4H**).
203 Quality control by principal component analysis (**Fig. 4I**) and hierarchical cluster of genes
204 showing high sample deviation (**Fig. 4J**) confirmed strong reproducibility of sample replicas.
205 Pathway analysis showed enrichment for GO terms linked to innate immune response,
206 mesodermal cell differentiation, and cell-cell adhesion in Ad-GFP-treated cells, whereas
207 neutrophil chemotaxis, extracellular matrix organization, and negative regulation of immune
208 response were enriched in Ad-Cre-treated cells (**Fig. 4K**). Ingenuity Pathway Analysis (IPA)
209 showed that the activated pathways in Ad-GFP-treated NMCCs are associated with the positive
210 regulation of migration and osteogenesis, including IL-3 signaling, JAK/STAT signaling, and
211 Erythropoietin signaling pathway (Z scores -2.236, -2, and -1.633; **Fig. 4L**) (*14-19*). Conversely,
212 upregulated signaling pathways in Ad-Cre-treated NMCCs were associated with the negative
213 regulation of cell migration and ossification, including IL-17 signaling as well as PTEN
214 signaling (Z scores 1.89 and 1; **Fig. 4L**) (*20-22*). These data further confirmed functional
215 differences previously observed among $p75^{fl/fl}$ and $p75^{PDGFR\alpha}$ mice, including the low migration
216 and osteogenic potential of *p75*-deficient calvarial stromal cells.

217

218 ***Macrophage-derived NGF regulates NMCC migration via p75 signaling***

219 Previously, we have shown that *Ngf* derived from LysM-expressing monocytes/macrophages is
220 essential for calvarial bone defect repair (*3*). To confirm this observation, Ngf^{LysM} mice were
221 again subjected to frontal bone injuries and compared to $Ngf^{fl/fl}$ control mice (**Fig. 5A**). Micro-
222 CT reconstructions and cross-sectional images within the defect site demonstrated impaired re-
223 ossification among Ngf^{LysM} mice in comparison to $Ngf^{fl/fl}$ mice (**Fig. 5B**). In order to investigate a
224 potential link between macrophage-derived NGF and stromal cell p75 signaling to enhance bone
225 regeneration, migration was assessed *in vitro* and *in vivo* using Ngf^{LysM} or $Ngf^{fl/fl}$ animals (**Fig.**
226 **5C-K**). Deletion of *Ngf* in $LysM^{+}$ monocytes/macrophages led to a prominent decrease in
227 stromal cell migration into the defect site, as assessed by PDGFRα immunostaining (**Fig. 5C**)
228 and flow cytometry for PDGFRα of the microdissected bone defect site (**Fig. 5D,E**). To directly
229 address the paracrine effects of macrophages on calvarial stromal cells, conditioned medium
230 (CM) experiments were performed, harvesting CM from either Ngf^{LysM} or $Ngf^{fl/fl}$ macrophages
231 (**Fig. 5F**). Results demonstrated that CM from macrophages derived from $Ngf^{fl/fl}$ mice promoted
232 cell migration assessed by scratch wound healing assay, but this pro-migratory effect was not
233 seen in NGF-depleted CM from Ngf^{LysM} macrophages (**Fig. 5G**). A similar result was observed
234 with invasion assays, in which $Ngf^{fl/fl}$ but not Ngf^{LysM} macrophage CM induced transwell
235 invasion (**Fig. 5H**). Next, the effects of macrophage CM were assayed on NMCCs derived from
236 $p75^{PDGFR\alpha}$ animals (**Fig. 5I,J**). After in vitro exposure to 4-Hydroxytamoxifen, a significant
237 reduction in *p75* expression was observed among $p75^{PDGFR\alpha}$ NMCCs (**Fig. 5I**). Among control
238 cells without 4-Hydroxytamoxifen treatment, macrophage CM again induced cellular migration.
239 Notably, induction of cellular migration by macrophage CM was not seen among *p75* knockout

240 calvarial cells (**Fig. 5J**). In sum, macrophage-derived NGF appears to promote mesenchymal
241 calvarial cell migration and bone healing via its low-affinity receptor p75.
242
243 ***Mesenchymal subpopulation changes macrophage phenotype and function through p75***
244 ***signaling***
245 In addition to terms linked to migration and wound healing, pathway analysis of scRNA-seq and
246 bulk RNA-seq revealed a recuring theme of altered immune processes in the context of *p75*
247 deletion (**Fig. 6A**). To investigate how mesenchymal *p75* deletion may affect immune cell
248 function, we examined the characteristics of mesenchymal subpopulations and found that
249 mesenchymal cluster 6 demonstrated DEGs enriched in several terms linked to immune cell
250 recruitment and function (**Fig. 6B**). This mesenchymal cluster 6 was found to express high levels
251 of inflammatory regulators, such as *Il1a*, *Il10*, and *Tnf*, which were found to have reduced
252 expression in cells derived from $p75^{\text{Pdgfr}\alpha}$ mice (**Fig. 6C**).
253
254 To determine whether a concomitant decrease was observed in macrophage signaling resulting
255 from this reduced mesenchymal expression of inflammatory markers, we next investigated
256 changes in macrophages within our scRNA sequencing of $p75^{\text{fl/fl}}$ and $p75^{\text{Pdgfr}\alpha}$ bone defects (**Fig.**
257 **6D-F**). While only a minor shift in overall population distribution was observed (**Fig. 6D, Fig.**
258 **S2B**), expression of markers linked to both M1 and M2 macrophage activation were inhibited
259 among $p75^{\text{Pdgfr}\alpha}$ mice in comparison to $p75^{\text{fl/fl}}$ mice (**Fig. 6E**). This was consistent with
260 reductions in inflammatory pathways among macrophages within $p75^{\text{Pdgfr}\alpha}$ defect sites, such as
261 TNFα, IL1, IL6, the complement pathway, and Toll-like receptor signaling (**Fig. 6F**). In order to
262 confirm this scRNA-seq data, macrophage number and activity were assessed by

263 immunohistochemistry within *p75*$^{fl/fl}$ and *p75*$^{Pdgfr\alpha}$ bone defect sections. First, a clear reduction in
264 F4/80^{+} (**Fig. 6G**) or CD68^{+} (**Fig. 6H**) macrophages was observed within *p75*$^{Pdgfr\alpha}$ mice. TNF-α
265 immunohistochemical staining was next performed, and confirmed a significant reduction across
266 the *p75*$^{Pdgfr\alpha}$ defect site (**Fig. 6I**). This diminished inflammatory setting was also associated with
267 a reduction of NGF immunoreactive cells with the *p75*$^{Pdgfr\alpha}$ defect site (**Fig. 6J**). In aggregate,
268 depletion of *p75* in PDGFRα-expressing mesenchymal cells significantly inhibits injury-
269 associated macrophage activation and NGF expression, associated with a delay in bone defect
270 repair.
271
272 ***p75 regulates human calvarial osteoblasts migration and osteogenesis***
273 Finally, the role of p75 in human cells and tissue samples was examined (**Fig. 7**). To investigate
274 the role of p75 in human calvarial osteoblasts, siRNA-mediated knockdown of *p75* was
275 performed (**Fig. 7A**). As in mouse NMCCs, knockdown of *p75* inhibited cell migration in
276 wound-healing and transwell assays (**Fig. 7B,C**) as well as impaired osteogenic differentiation
277 (**Fig. 7D,E**). Next, detection of p75 expression was observed across human fracture calluses
278 (**Fig. 7F**). In similarity to findings in mouse calvaria, p75 was abundantly expressed in bone
279 lining cells of the fracture callus, especially in Osteocalcin^{+} bone lining osteoblasts (**Fig.
280 7G,H**). Thus, *p75* in osteoblasts and their cellular precursors is essential for cell migration and
281 bone repair – a finding conserved across mouse and human tissues.
282
283 **Discussion**
284 In this study, we sought to define the cellular and molecular events that accompany bone repair
285 in genetic mouse models that enabled specific disruption of NGF-p75 signaling components in

286 bone. We show that NGF derived from myelomonocytic cells is acutely upregulated following
287 bone injury, triggering a migration of p75-expressing mesenchymal cells into the damaged area.
288 When this signaling pathway is disrupted, defective cellular migration, ossification, and a
289 secondary blunting of the immune response are the result. Given these observations, it is not
290 clear as to why experimental work with neutralizing antibodies to NGF have not shown a
291 significant delay in bone healing (*23, 24*). It is probable that the analgesic effects of anti-NGF are
292 observed at a lower dose than those needed to impede tissue repair. Nevertheless, when taken
293 together with our past work, these data illustrate the multimodal and critical effects of NGF in
294 bone repair, including coordinating proper mesenchymal cell migration, re-innervation and
295 vascularization, and ossification – cellular functions which are regulated in concert via both NGF
296 receptors.
297
298 Our studies focused on the role of p75 in mesenchymal progenitors and osteoblasts by using
299 available transgenic animals. However, p75 expression is of course present in other cell types,
300 including pericytes and immune cells. For example, proNGF-p75 signaling in the vasculature,
301 including pericytes and endothelial cells, has been shown to mediate vascular response to injury
302 of either the myocardium or injured limb in ischemia-reperfusion models (*25-27*). Our
303 observations on unchanged vascularity in the context of *p75* conditional gene deletion thus likely
304 stems from the choice of Cre driver. Likewise, macrophages are also responsive to the
305 chemotactic properties of proNGF via the low-affinity receptor p75 (*28*). Thus, it is possible that
306 p75 has more functional roles in tissue repair than would be illustrated by our experimental
307 design. Second, our studies were focused on a single neurotrophin given our laboratories'
308 interests and past work in this area (*2-4, 29*). Nevertheless, other neurotrophins such as BDNF

309 (Brain derived neurotrophic factor) are also expressed in human fracture sites including in
310 endothelial and osteoblastic cells during early repair phases (*30*). It is likely that several
311 neurotrophins have functionally redundant roles in regulating p75-mediated tissue ingrowth after
312 bone injury – a hypothesis that has not yet been analyzed experimentally.
313
314 The extent to which NGF signaling can be targeted therapeutically for its beneficial effects on
315 bone and bone repair represents an evolving area of interest in the orthopaedic research
316 community. Several recent papers suggest that positive regulation of NGF-TrkA signaling may
317 have beneficial effects in long bone fracture repair. For example, local injection of NGF
318 stimulated early fracture maturation in a closed tibial fracture mouse model (*31*). Systemic
319 administration of the partial TrkA agonist Gambogic amide has been used to improve indices of
320 fibular fracture healing in mice (*32*), and analogously to augment skeletal adaptation to
321 mechanical load (*33*). Our present study demonstrates the multiple cell specific functions that
322 NGF signaling plays in bone repair. In combination with past work (*2, 3*), we document clear
323 and potentially synergistic roles for proNGF-p75 and NGF-TrkA signaling in osseous repair.
324

325 **Materials and Methods**

326 ***Mice***

327 All animal experiments were performed according to approved protocols (MO16M226 &
328 MO19M366) of the Animal Care and Use Committee (ACUC) at Johns Hopkins University
329 (JHU). Pdgfrα-CreER^{TM} animals were a kind gift from the Dwight Bergles laboratory (*34*) and
330 are commercially available (The Jackson Laboratory, Stock No. 018280, Bar Harbor, ME). OC-
331 Cre animals were generated by the Clemens laboratory and are commercially available (JAX

332 Stock No. 019509). Pdgfrα$^{mT/mG}$ or OC$^{mT/mG}$ mice were obtained by crossing Pdgfrα-CreER^{TM} or
333 OC-Cre with mT/mG mice (JAX Stock No. 007576). *p75*$^{PDGFR\alpha}$ or *p75*^{OC} mice were obtained by
334 crossing Pdgfrα$^{mT/mG}$ or OC$^{mT/mG}$ mice with *p75*$^{fl/fl}$ mice (JAX Stock No. 031162). Tamoxifen
335 (TM; Sigma-Aldrich, St. Louis, MO) was dissolved in sunflower seed oil (Sigma-Aldrich) and
336 injected intraperitoneally according to previously validated protocols (TM: 150 mg/kg/d for 5 d)
337 (*12, 35*). LysM-Cre mice were purchased from the Jackson Laboratory (JAX Stock No. 004781).
338 In order to achieve cell specific deletion of *Ngf*, *Ngf*^{LysM} were obtained by crossing LysM-Cre
339 animals with *Ngf*$^{fl/fl}$ animals. When feasible, littermate analysis was performed by investigators
340 blinded to the mouse genotype. All these lines were backcrossed for at least 8 generations to the
341 C57BL/6J background before used for the experiments reported here.
342

343 ***Calvarial defect procedures***

344 Calvarial defects were performed based on our prior methods (*3, 35, 36*). In Pdgfrα$^{mT/mG}$ or
345 *p75*$^{PDGFR\alpha}$ mice, TM administration was performed 14 d prior to defect creation as previously
346 validated (*12, 35*). Mice were provided isoflurane (2-3% inh) and Buprenorphine (1 mg/kg sc).
347 Briefly, hair overlying the calvaria was clipped, and a 1 cm skin incision was made over the
348 midline skull to expose the frontal bone. Next, a 1.8 mm diameter, full-thickness, circular
349 frontal bone defect was created in the non-suture associated frontal bone (right side) using a
350 micro surgical drill and a trephine drill bit. Meticulous care was taken to protect the neighboring
351 sutures and the underlying dura mater. Finally, the skin was sutured and the animals were
352 monitored per established postoperative protocols. Mice were euthanized after 7 d or 28 d for
353 analysis.

354

355 ***Radiographic analyses***

356 Skulls were fixed in 4% paraformaldehyde (PFA) for 24 h and evaluated using a high-resolution
357 micro-CT imaging system (SkyScan 1275; Bruker, Kontich, Belgium). Scans were obtained at
358 an image resolution of 12 μm and set as 1 mm of aluminum filter, X-ray voltage of 65 kVP,
359 anode current of 153 μA, exposure time of 160-218 ms, frame averaging of 6, and rotation step
360 of 0.3 degrees. Three-dimensional images were then reconstructed from the 2D X-ray projections
361 using a commercial software NRecon software (v1.7.0.4, SkyScan). For 3D morphometric
362 analyses of images, CTAn software (v1.16, SkyScan), CTVol (v2.0, SkyScan), and CTVox
363 (v3.2, SkyScan) were used. For calvarial defect analysis, a cylindrical volume of interest
364 centered around each defect site was defined as the 1.8 mm in diameter and 1.2 mm in height
365 with a threshold value of 70-255. Bone volume (BV) and fractional bone volume (bone
366 volume/tissue volume (BV/TV)) were calculated from binary x-ray images. Bone fractional area
367 (BFA) and defect diameter were calculated by using CTVox to create a 3D rendering of calvarial
368 defect and measuring by ImageJ software (Version 1.8.0; NIH, Bethesda, MD). Lastly, a bone
369 healing score from 0 to 4 was assigned by three blinded observers according to previously
370 published grading scales for calvarial defect healing (*13*).

371

372 ***Histology and immunohistochemistry***

373 After radiographic imaging, samples were decalcified in 14% EDTA for 21 days, embedded in
374 optimal cutting temperature compound (OCT; Sakura, Torrance, CA), and sectioned in a coronal
375 plane at 20 or 50 um thickness. H&E staining was performed on serial sections. For
376 immunofluorescent staining, all sections were incubated with trypsin enzymatic antigen retrieval

377 solution (Abcam, Cambridge, MA, USA) for 3 min at room temperature (RT). When 50 μm
378 sections were used, sections were next permeabilized with 0.5% Triton-X for 30 min. All
379 sections were blocked with 5% goat or donkey serum in PBS for 1 h at RT and incubated with
380 the primary antibodies (see **Table S1** for a summary of antibodies used) at 37 °C for 3 h or
381 overnight at 4 °C. Next, secondary antibodies (1:200) were used with incubation for 2 h at RT.
382 Sections were counterstained with DAPI mounting medium (Vector laboratories, Burlingame,
383 CA). All histological sections were examined under a Zeiss 800 confocal microscope (Zeiss,
384 Thornwood, NY) or Leica DM6 microscope (Leica Microsystems Inc, Wetzlar, Germany).
385 Staining without primary antibody was used to exclude non-specific staining. For visualization
386 of reporter activity, a wildtype specimen prepared in the same fashion was used as a control to
387 identify the intensity of autofluorescence. Images were quantified using ImageJ or Imaris
388 (Bitplane, Belfast, UK) software. For the lineage tracing of cell migration, the percentage of
389 PDGFRα^+ cells was calculated in the central defect region. For the TUBB3 staining, the volume
390 of TUBB3$^+$ nerve fibers was quantified with three different sites of the defect span and the
391 average value was taken as the final value of the sample. For all other immunohistochemistry,
392 the fluorescence intensity was quantified on the edges of bone in single microscopical fields.
393

394 ***Isolation and culture of neonatal mouse calvarial cells***

395 Primary neonatal mouse calvarial cells (NMCCs) were collected from *p75*$^{fl/fl}$ or *p75*$^{PDGFR\alpha}$
396 embryos at postnatal day 2. Frontal and parietal bones were minced and subjected to six
397 sequential enzymatic digestions with a mixture containing 1 mg/mL collagenase type I
398 (Worthington Biochemical Corporation, Lakewood, NJ; LS004197) and 1 mg/mL collagenase
399 type II (Worthington Biochemical Corporation; LS004177) (*37*). Cell fractions (from sequential

400 digestions 3-6) were collected and cultured in α-MEM supplemented with 15% (vol/vol) FBS,
401 100 U/mL penicillin, and 100 mg/mL streptomycin. In select experiments, *p75*$^{fl/fl}$ NMCCs were
402 exposed to an adenovirus encoding either Cre Recombinase (Ad-Cre, multiplicity of
403 infection=150; 1045-HT, Vector Biosystems, Malvern, PA) or GFP (Ad-GFP, multiplicity of
404 infection=150; 1060-HT, Vector Biosystems). In additional select experiments, *p75*$^{PDGFR\alpha}$
405 NMCCs were treated with 4-Hydroxytamoxifen (2 μM) or vehicle control (Sigma-Aldrich).
406
407 ***Proliferation***
408 Proliferation assays were performed in 96 well plates (2×10^3 NMCCs/well) and assayed at 48 h
409 using the CellTiter96® AQueous One Solution Cell Proliferation Assay kit (MTS; Promega,
410 Madison, WI) (*38*). Briefly, 20 µl of MTS solution was added to each well. After incubation for
411 1 h at 37 °C, the plate was measured using an Epoch microspectrophotometer (BioTek,
412 Winooski, VT) by absorbance at 490 nm.
413
414 ***Isolation of mouse macrophages and macrophage conditioned medium***
415 Macrophages were collected from *Ngf*$^{fl/fl}$ or *Ngf*^{LysM} mice (8 weeks old mixed gender animals).
416 Bone marrow cells were flushed from the long bones (femur and tibia) with culture medium and
417 resuspended in medium containing macrophage colony-stimulating factor (M-CSF; 15 ng/mL)
418 (*39*). After 7 d in culture, adherent bone marrow-derived macrophages were incubated in growth
419 medium without M-CSF for 2 d and the supernatant was collected for conditioned medium
420 experiments.
421
422 ***Migration***

423 Cell migration was measured with Ibidi inserts (Ibidi, Planegg/Martinsried, Germany), where 2 ×
424 10^4 NMCCs were seeded and grown to confluency. Inserts were removed and cell migration into
425 the empty area was monitored by brightfield microscopy at 0 or 14 h. The equilibrium width of
426 the gap was calculated using the ImageJ software. Here, gap closure = (scratch area at hour 0 −
427 scratch area at hr 14)/scratch area at hr 0 × 100%. For the transwell migration assays, 2.0 × 10^4
428 NMCCs were resuspended in 100 μL of α-MEM medium without FBS and were placed in the
429 upper well of 8-μm pore-size Transwell 24-insert plates (Corning, NY). The migration assay was
430 performed by adding to the bottom well 600 μL of α-MEM medium supplemented with 15%
431 FBS or conditioned medium from cultured macrophages. After 4 h, cells on the bottom of the
432 inserts were fixed and stained with 0.5% crystal violet (Sigma-Aldrich) for 15 min. Pictures were
433 taken by using 100× magnification (Leica Microsystems Inc). Crystal violet was eluted using
434 33% acetic acid, and the eluent quantified by absorbance at 570 nm.
435
436 ***Osteogenic differentiation***
437 NMCCs were seeded in 24-well plates at a density of 1 × 10^5 cells/well. Osteogenic
438 differentiation medium (ODM) consisted of α-MEM, 10% FBS, 1% penicillin/streptomycin with
439 100 nM dexamethasone, 50 μM ascorbic acid and 10 mM β-glycerophosphate (*40-42*). 24 h after
440 cell seeding, growth medium was replaced with ODM, replenished every 3-4 d. For alizarin red
441 (AR) staining, cells were fixed with 4% paraformaldehyde and stained with a 2% alizarin red
442 solution at 14 d of differentiation. Pictures were taken using Olympus Epson scanner (Los
443 Angeles, CA), followed by incubation with 0.1 N sodium hydroxide and quantified using an
444 Epoch microspectrophotometer (BioTek) by absorbance at 548 nm.
445

446 ***Ribonucleic acid isolation and quantitative real-time polymerase chain reaction***

447 Total RNA was extracted from the cultured cells using TRIzol Reagent (Invitrogen, Carlsbad,
448 CA, USA) according to the manufacturer's instructions. 1 μg of total RNA was used for reverse
449 transcription with iScript™ cDNA synthesis kit (Bio-Rad, Hercules, CA) following
450 manufacturer's instructions. Real-time PCR was performed using SYBR™ Green PCR Master
451 Mix (ThermoFisher Scientific, Waltham, MA) according to the manufacturer's protocol.
452 Relative gene expression was calculated using a $2^{-\Delta\Delta Ct}$ method by normalization with *GAPDH*.
453 Primer sequences are presented in **Table S2**.

454

455 ***Transcriptomics***

456 The RNA content of Ad-Cre and Ad-GFP treated NMCCs was detected by total RNA
457 sequencing. Briefly, *p75*$^{fl/fl}$ NMCCs were exposed to Ad-Cre or Ad-GFP (multiplicity of
458 infection=150) for 72h, then total RNA was extracted from Ad-Cre and Ad-GFP treated *p75*$^{fl/fl}$
459 NMCCs by Trizol (Life technologies corporation, Gaitherburg, MD). The RNA samples were
460 sent to the JHMI Transcriptomics and Deep Sequencing Core and quantified by deep sequencing
461 with the Illumina NextSeq 500 platform (Illumina, San Diego, CA). Data analyses were
462 performed using software packages including Partek Genomics Suite, Spotfire DecisionSite for
463 Functional Genomics, QIAGEN Ingenuity® Pathway Analysis, and DAVID bioinformatics
464 resources (*43*).

465

466 ***Apoptosis detection***

467 Ad-Cre and Ad-GFP treated *p75*$^{fl/fl}$ NMCCs were seeded in Millicell EZ SLIDE
468 (MilliporeSigma, Burlington, MA) and cultured for 24 h. The cells were fixed in 4% PFA for 15

469 min and permeabilized with 0.25% Triton X-100 for 20 min. TUNEL assay was carried out
470 using the Click-iT Plus TUNEL Assay for in situ apoptosis detection with Alexa Fluor 647 dyes
471 (ThermoFisher Scientific). Pictures were taken using a Leica DM6 microscope.
472

473 ***Flow cytometry analysis***

474 In order to detect cell migration *in vivo*, skull defects were microdissected 7 days after injury.
475 The cells in the defect site were obtained by collagenase Type I/II (1 mg/mL) digestion using the
476 above method. Briefly, cell fractions (from sequential digestions 1-6) were collected and
477 resuspended in red blood cell lysis buffer (37°C for 5 min). After centrifugation, cells were
478 resuspended in Hanks' Balanced Salt Solution (HBSS) and 0.5% bovine serum albumin. The
479 resulting cells was further processed for cell sorting, using a mixture of the following directly
480 conjugated antibodies (**Table S1**): anti-CD31-allophycocyanin (1:30), anti-CD45-
481 allophycocyanin (1:30), anti-Ter119-allophycocyanin (1:30), anti-PDGFRα-BV421 (1:50) were
482 added separately and incubated at 4°C for 20 min. Cells were then washed with PBS and
483 examined with a DakoCytomation MoFlo (Beckman, Indianapolis, IN). FlowJo software (Tree
484 Star Inc., Ashland, OR) was used for the analysis of flow cytometry data. Gating and PDGFRα
485 frequency were set in relation to matching isotype control.
486

487 ***Single-cell RNA sequencing***

488 Skulls were microdissected 7 days after defect creation and digested with collagenase Type I/II
489 (1 mg/mL) digestion using the above method. Cell fractions (from sequential digestions 1-6)
490 were collected and resuspended in red blood cell lysis buffer (37°C for 5 min). Digestions were
491 subsequently filtered through 40μm sterile strainers. Cells were then washed in PBS and

492 resuspended in HBSS at a concentration of ~1000 cells/μl. Cell viability was assessed with
493 Trypan blue exclusion on a Countess II (ThermoFisher Scientific) automated counter and
494 showed a >85% viability. Cells were sent to the JHMI Transcriptomics and Deep Sequencing
495 Core. The library was generated using the 10X Genomics chromium controller following the
496 manufacturers protocol. Cell suspensions were loaded onto a Chromium Single Cell A chip
497 along with reverse transcription (RT) master mix and single cell 3' gel beads, aiming for 10,000
498 cells per channel. Following generation of single-cell gel bead-in-emulsions (GEMs), reverse
499 transcription was performed and the resulting Post GEM-RT product was cleaned up using
500 DynaBeads MyOne Silane beads. Beads are provided by 10X with the kit. The cDNA was
501 amplified, SPRIselect (Beckman Coulter, Brea, CA) cleaned and quantified then enzymatically
502 fragmented and size selected using SPRIselect beads to optimize the cDNA amplicon size prior
503 to library construction. An additional round of double-sided SPRI bead cleanup is performed
504 after end repair and A-tailing. Fragmentation, end repair and a-tailing are all one reaction,
505 followed by the double sided cleanup. Another single-sided cleanup is done after adapter
506 ligation. Indexes were added during PCR amplification and a final double-sided SPRI cleanup
507 was performed. Libraries were quantified by Kapa qPCR for Illumina Adapters (Roche) and size
508 was determined by Agilent Bioanalyzer 2100. Read 1 primer, read 2 primer, P5, P7, and sample
509 indices were incorporated per standard GEM generation and library construction via end repair,
510 A-tailing, adaptor ligation and PCR. Libraries were generated with unique sample indices (SI)
511 for each sample. Libraries were sequenced on an Illumina NovaSeq SP 100 cycle (San Diego,
512 CA). *CellRanger* was used to perform sample de-multiplexing, barcode processing, and single
513 cell gene counting (Alignment, Barcoding and UMI Count) at the JHMI Transcriptomics and
514 Deep Sequencing Core. Downstream analysis steps were performed using *Seurat*. Cells were

515 first filtered to have >500 and <8,000 detected genes, as well as less than 20% mitochondrial
516 transcripts. *SCTransform*, including regression for cell cycle scores derived using the
517 *CellCycleScoring* function, and dimensional reductions using uniform manifold approximation
518 and projection (UMAP) was performed using *Seurat*. Pathway activation scores were generated
519 using the *AddModuleScore* function of *Seurat* using validated gene lists from KEGG pathways.
520

521 ***Statistical analysis***

522 Data are presented as the mean ± one standard deviation (SD). Statistical analyses were
523 performed using GraphPad Prism (Version 7.0) or R package *ggpubr*. *In vitro* experiments were
524 performed in biologic and experimental triplicate. The number of animals used in the *in vivo*
525 experiments are shown in figure legends. For cell depletion experiments, our depletion efficiency
526 resulted in effect sizes of 1.75 or higher. For these scenarios, with at least 4 mice per group, a
527 two-sample t test would provide 80% power to detect effect sizes of at least 1.75, assuming a
528 two-sided 0.05 level of significance. The Kolmogorov–Smirnov test was used to confirm normal
529 distribution of the data. A two-tailed Student's *t* test or Wilcoxon test was used for two group
530 comparisons. One-way and two-way ANOVA tests were used for multiple groups, followed by
531 Tukey's multiple comparisons test. *$P<0.05$, **$P<0.01$, and ***$P<0.001$ were considered
532 significant.
533

534 **References**

535 1. J. W. Ferguson, R. P. Atit, A tale of two cities: The genetic mechanisms governing
536 calvarial bone development. *Genesis* **57**, e23248 (2019).
537 2. Z. Li *et al.*, Fracture repair requires TrkA signaling by skeletal sensory nerves. *J Clin*
538 *Invest* **129**, 5137-5150 (2019).
539 3. C. A. Meyers *et al.*, A Neurotrophic Mechanism Directs Sensory Nerve Transit in Cranial
540 Bone. *Cell Rep* **31**, 107696 (2020).

541 4. R. E. Tomlinson *et al.*, NGF-TrkA Signaling by Sensory Nerves Coordinates the
542 Vascularization and Ossification of Developing Endochondral Bone. *Cell Rep* **16**, 2723-
543 2735 (2016).
544 5. M. Alvarez-Viejo, Y. Menendez-Menendez, J. Otero-Hernandez, CD271 as a marker to
545 identify mesenchymal stem cells from diverse sources before culture. *World J Stem Cells*
546 **7**, 470-476 (2015).
547 6. C. A. Bentley, K. F. Lee, p75 is important for axon growth and schwann cell migration
548 during development. *J Neurosci* **20**, 7706-7715 (2000).
549 7. B. Wang *et al.*, Depressed Langerhans cell migration and reduced contact
550 hypersensitivity response in mice lacking TNF receptor p75. *J Immunol* **159**, 6148-6155
551 (1997).
552 8. T. Redmer *et al.*, The nerve growth factor receptor CD271 is crucial to maintain
553 tumorigenicity and stem-like properties of melanoma cells. *PLoS One* **9**, e92596 (2014).
554 9. J. Radke, F. Rossner, T. Redmer, CD271 determines migratory properties of melanoma
555 cells. *Sci Rep* **7**, 9834 (2017).
556 10. N. H. Molloy, D. E. Read, A. M. Gorman, Nerve growth factor in cancer cell death and
557 survival. *Cancers (Basel)* **3**, 510-530 (2011).
558 11. S. Wislet, G. Vandervelden, B. Rogister, From Neural Crest Development to Cancer and
559 Vice Versa: How p75(NTR) and (Pro)neurotrophins Could Act on Cell Migration and
560 Invasion? *Front Mol Neurosci* **11**, 244 (2018).
561 12. Y. Wang *et al.*, PDGFRalpha marks distinct perivascular populations with different
562 osteogenic potential within adipose tissue. *Stem cells* **38**, 276-290 (2020).
563 13. P. P. Spicer *et al.*, Evaluation of bone regeneration using the rat critical size calvarial
564 defect. *Nat Protoc* **7**, 1918-1929 (2012).
565 14. A. Barhanpurkar-Naik, S. T. Mhaske, S. T. Pote, K. Singh, M. R. Wani, Interleukin-3
566 enhances the migration of human mesenchymal stem cells by regulating expression of
567 CXCR4. *Stem Cell Res Ther* **8**, 168 (2017).
568 15. A. P. Barhanpurkar *et al.*, IL-3 promotes osteoblast differentiation and bone formation in
569 human mesenchymal stem cells. *Biochem Biophys Res Commun* **418**, 669-675 (2012).
570 16. D. L. Silver, E. R. Geisbrecht, D. J. Montell, Requirement for JAK/STAT signaling
571 throughout border cell migration in Drosophila. *Development* **132**, 3483-3492 (2005).
572 17. J. Li, JAK-STAT and bone metabolism. *JAKSTAT* **2**, e23930 (2013).
573 18. A. Mirmohammadsadegh *et al.*, Role of erythropoietin receptor expression in malignant
574 melanoma. *J Invest Dermatol* **130**, 201-210 (2010).
575 19. J. Kim *et al.*, Erythropoietin mediated bone formation is regulated by mTOR signaling. *J*
576 *Cell Biochem* **113**, 220-228 (2012).
577 20. J. Chang *et al.*, NF-kappaB inhibits osteogenic differentiation of mesenchymal stem cells
578 by promoting beta-catenin degradation. *Proc Natl Acad Sci U S A* **110**, 9469-9474
579 (2013).
580 21. K. Tian, R. Di, L. Wang, MicroRNA-23a enhances migration and invasion through
581 PTEN in osteosarcoma. *Cancer Gene Ther* **22**, 351-359 (2015).
582 22. A. R. Guntur, M. I. Reinhold, J. Cuellar, Jr., M. C. Naski, Conditional ablation of Pten in
583 osteoprogenitors stimulates FGF signaling. *Development* **138**, 1433-1444 (2011).
584 23. N. J. Koewler *et al.*, Effects of a monoclonal antibody raised against nerve growth factor
585 on skeletal pain and bone healing after fracture of the C57BL/6J mouse femur. *J Bone*
586 *Miner Res* **22**, 1732-1742 (2007).

587 24. A. E. Rapp *et al.*, Analgesia via blockade of NGF/TrkA signaling does not influence
588 fracture healing in mice. *J Orthop Res* **33**, 1235-1241 (2015).
589 25. J. Fang *et al.*, Recombinant Extracellular Domain (p75ECD) of the Neurotrophin
590 Receptor p75 Attenuates Myocardial Ischemia-Reperfusion Injury by Inhibiting the p-
591 JNK/Caspase-3 Signaling Pathway in Rat Microvascular Pericytes. *J Am Heart Assoc* **9**,
592 e016047 (2020).
593 26. A. Caporali *et al.*, p75(NTR)-dependent activation of NF-kappaB regulates microRNA-
594 503 transcription and pericyte-endothelial crosstalk in diabetes after limb ischaemia. *Nat*
595 *Commun* **6**, 8024 (2015).
596 27. C. J. Siao *et al.*, ProNGF, a cytokine induced after myocardial infarction in humans,
597 targets pericytes to promote microvascular damage and activation. *J Exp Med* **209**, 2291-
598 2305 (2012).
599 28. K. S. Williams, D. A. Killebrew, G. P. Clary, J. A. Seawell, R. B. Meeker, Differential
600 regulation of macrophage phenotype by mature and pro-nerve growth factor. *J*
601 *Neuroimmunol* **285**, 76-93 (2015).
602 29. R. E. Tomlinson *et al.*, NGF-TrkA signaling in sensory nerves is required for skeletal
603 adaptation to mechanical loads in mice. *Proc Natl Acad Sci U S A* **114**, E3632-E3641
604 (2017).
605 30. O. Kilian *et al.*, BDNF and its TrkB receptor in human fracture healing. *Ann Anat* **196**,
606 286-295 (2014).
607 31. K. O. Rivera *et al.*, Local injections of beta-NGF accelerates endochondral fracture repair
608 by promoting cartilage to bone conversion. *Sci Rep* **10**, 22241 (2020).
609 32. M. R. Johnstone *et al.*, The selective TrkA agonist, gambogic amide, promotes
610 osteoblastic differentiation and improves fracture healing in mice. *J Musculoskelet*
611 *Neuronal Interact* **19**, 94-103 (2019).
612 33. G. Fioravanti, P. Q. Hua, R. E. Tomlinson, The TrkA agonist gambogic amide augments
613 skeletal adaptation to mechanical loading. *Bone* **147**, 115908 (2021).
614 34. S. H. Kang, M. Fukaya, J. K. Yang, J. D. Rothstein, D. E. Bergles, NG2+ CNS glial
615 progenitors remain committed to the oligodendrocyte lineage in postnatal life and
616 following neurodegeneration. *Neuron* **68**, 668-681 (2010).
617 35. J. Xu *et al.*, Human perivascular stem cell-derived extracellular vesicles mediate bone
618 repair. *eLife* **8**, (2019).
619 36. C. S. Lee, G. C. Hsu, T. Sono, M. Lee, A. W. James, Development of a Biomaterial
620 Scaffold Integrated with Osteoinductive Oxysterol Liposomes to Enhance Hedgehog
621 Signaling and Bone Repair. *Mol Pharm* **18**, 1677-1689 (2021).
622 37. K. Noda, M. Kitami, K. Kitami, M. Kaku, Y. Komatsu, Canonical and noncanonical
623 intraflagellar transport regulates craniofacial skeletal development. *Proc Natl Acad Sci U*
624 *S A* **113**, E2589-2597 (2016).
625 38. J. Xu *et al.*, Comparison of skeletal and soft tissue pericytes identifies CXCR4(+) bone
626 forming mural cells in human tissues. *Bone Res* **8**, 22 (2020).
627 39. X. Zhang, R. Goncalves, D. M. Mosser, The isolation and characterization of murine
628 macrophages. *Curr Protoc Immunol* **Chapter 14**, Unit 14 11 (2008).
629 40. J. Xu *et al.*, Lysosomal protein surface expression discriminates fat- from bone-forming
630 human mesenchymal precursor cells. *Elife* **9**, (2020).
631 41. Y. Wang *et al.*, Anti-DKK1 Enhances the Early Osteogenic Differentiation of Human
632 Adipose-Derived Stem/Stromal Cells. *Stem Cells Dev* **29**, 1007-1015 (2020).

42. S. Negri *et al.*, Systemic DKK1 neutralization enhances human adipose-derived stem cell mediated bone repair. *Stem Cells Transl Med* **10**, 610-622 (2021).
43. W. Huang da, B. T. Sherman, R. A. Lempicki, Systematic and integrative analysis of large gene lists using DAVID bioinformatics resources. *Nat Protoc* **4**, 44-57 (2009).

Acknowledgments

We thank the JHU microscopy core facility, JHMI deep sequencing and microarray core facility, and Hao Zhang within the JHU Bloomberg Flow Cytometry and Immunology Core.

Funding:

National Institutes of Health grant R21 DE027922 (Aaron W. James, Thomas L. Clemens)

National Institutes of Health grant R01 AR070773 (Aaron W. James)

Department of Defense grant USAMRAA W81XWH-18-1-0336 (Aaron W. James)

Department of Defense grant USAMRAA W81XWH-18-1-0121 (Aaron W. James)

Department of Defense grant USAMRAA W81XWH-20-1-0795 (Aaron W. James)

Department of Defense grant USAMRAA W81XWH-20-1-0302 (Aaron W. James)

American Cancer Society Research Scholar Grant (Aaron W. James)

American Cancer Society grant RSG-18-027-01-CSM (Aaron W. James)

the Maryland Stem Cell Research Foundation (Aaron W. James)

The content is solely the responsibility of the authors and does not necessarily represent the official views of the National Institute of Health or Department of Defense.

Author contributions:

Conceptualization: JX, ZL, RJT, AWJ

660 Methodology: JX, ZL, SN, YW, CAM, TS, QQ

661 Investigation: EFM

662 Visualization: RJT, AL

663 Supervision: TLC, AWJ

664 Writing—original draft: JX, RJT, AWJ

665 Writing—review & editing: TLC, AWJ

666

667 **Competing interests:** A.W.J. is a paid consultant for Novadip and Lifesprout LLC. This

668 arrangement has been reviewed and approved by the Johns Hopkins University in

669 accordance with its conflict of interest policies.

670

671 **Data and materials availability:** Expression data that support the findings of this study

672 have been deposited in Gene Expression Omnibus (GEO).

673

674 **Figures and Tables**

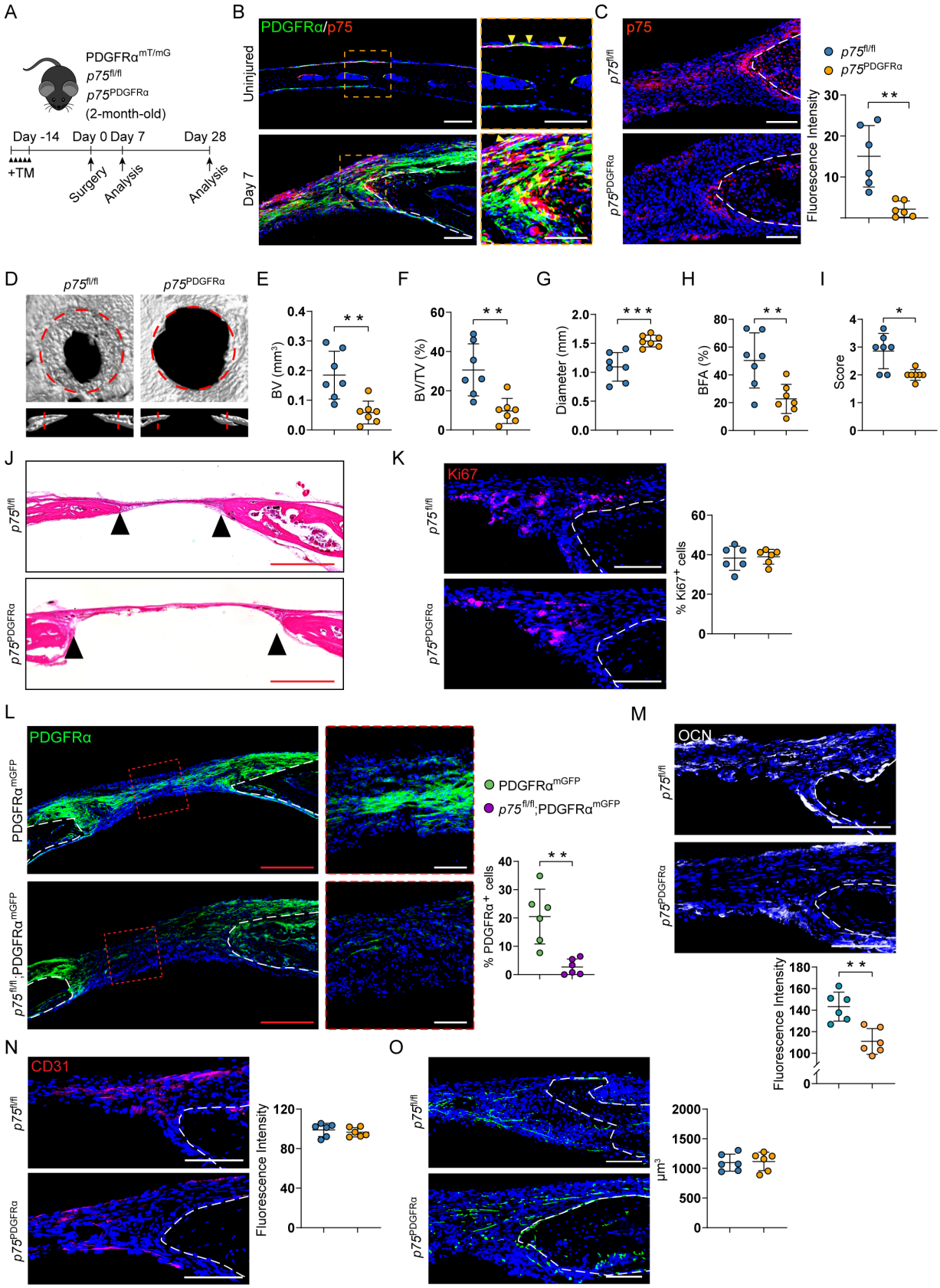

675

676 **Fig. 1. Deletion of *p75* in Pdgfrα-expressing cells impairs stromal cell migration and**
677 **calvarial bone defect repair. (A)** Schematic of experiment, in which *p75*$^{fl/fl}$ or *p75*^{PDGFRα}
678 animals (male, 2 mo old) were administered tamoxifen (TM), followed by frontal bone injury
679 (circular calvarial defect, 1.8 mm diameter) after 14 d, with analysis performed 7 or 28 d post-
680 operatively. **(B)** Immunohistochemistry for p75, appearing red, on the uninjured or calvarial
681 injury site (d 7 post-injury) within PDGFRα^{mGFP} reporter sections. White dashed lines indicate
682 bone edges. Yellow arrowheads indicate p75 and PDGFRα colocalization. TdTomato not shown.
683 **(C)** Validation of *p75* deletion by p75 immunohistochemistry and semi-quantitative analysis in
684 either *p75*$^{fl/fl}$ or *p75*^{Pdgfrα} mice, d7 post-injury. **(D)** Micro-CT reconstructions of the defect site in
685 a top down view (above) and coronal cross sectional images (below) among *p75*$^{fl/fl}$ and *p75*^{Pdgfrα}
686 animals, 28 d post-injury. Margins of original defect are indicated by dashed red lines. **(E-I)**
687 Micro-CT quantification of bone healing among *p75*$^{fl/fl}$ and *p75*^{Pdgfrα} mice (28 d post-injury),
688 including **(E)** Bone volume (BV), **(F)** Bone volume/tissue volume (BV/TV), **(G)** residual defect
689 diameter, **(H)** Bone formation area (BFA), and **(I)** Bone healing score. **(J)** H&E staining of
690 coronal cross-section of the healing defect site from *p75*$^{fl/fl}$ and *p75*^{Pdgfrα} mice. Black arrowheads
691 indicate healing bone edges. **(K)** Cellular proliferation at the bone defect edge, as assessed by
692 Ki67 immunofluorescent staining. Dashed white lines indicate bone edge. **(L)** Mesenchymal cell
693 migration, as assessed by Pdgfrα-CreER; mT/mG cell lineage tracing. Tile scan (left) and high-
694 magnification images of the central defect (right) demonstrate migration of GFP^{+} (PDGFRα^{mGFP})
695 progenitor cells into the defect site at d7 post-injury. Tdtomato is not shown. **(M-O)**
696 Immunohistochemical staining and semi-quantitative analysis of Osteocalcin (OCN) **(M)**, CD31
697 **(N)**, and Beta III Tubulin (TUBB3) **(O)** within the calvarial defect, d28 post-injury. Dashed
698 white lines indicate bone edge. In graphs, each dot represents a single animal. Red scale bar: 500
699 μm. White scale bar: 100 μm. N=3 mice per group for **(B)** and N=6-7 mice per group for **(C-O)**.
700 Data are represented as mean ± 1 SD. *$P<0.05$, **$P<0.01$, and ***$P<0.001$ as assessed using a
701 two-tailed Student's *t*-test.

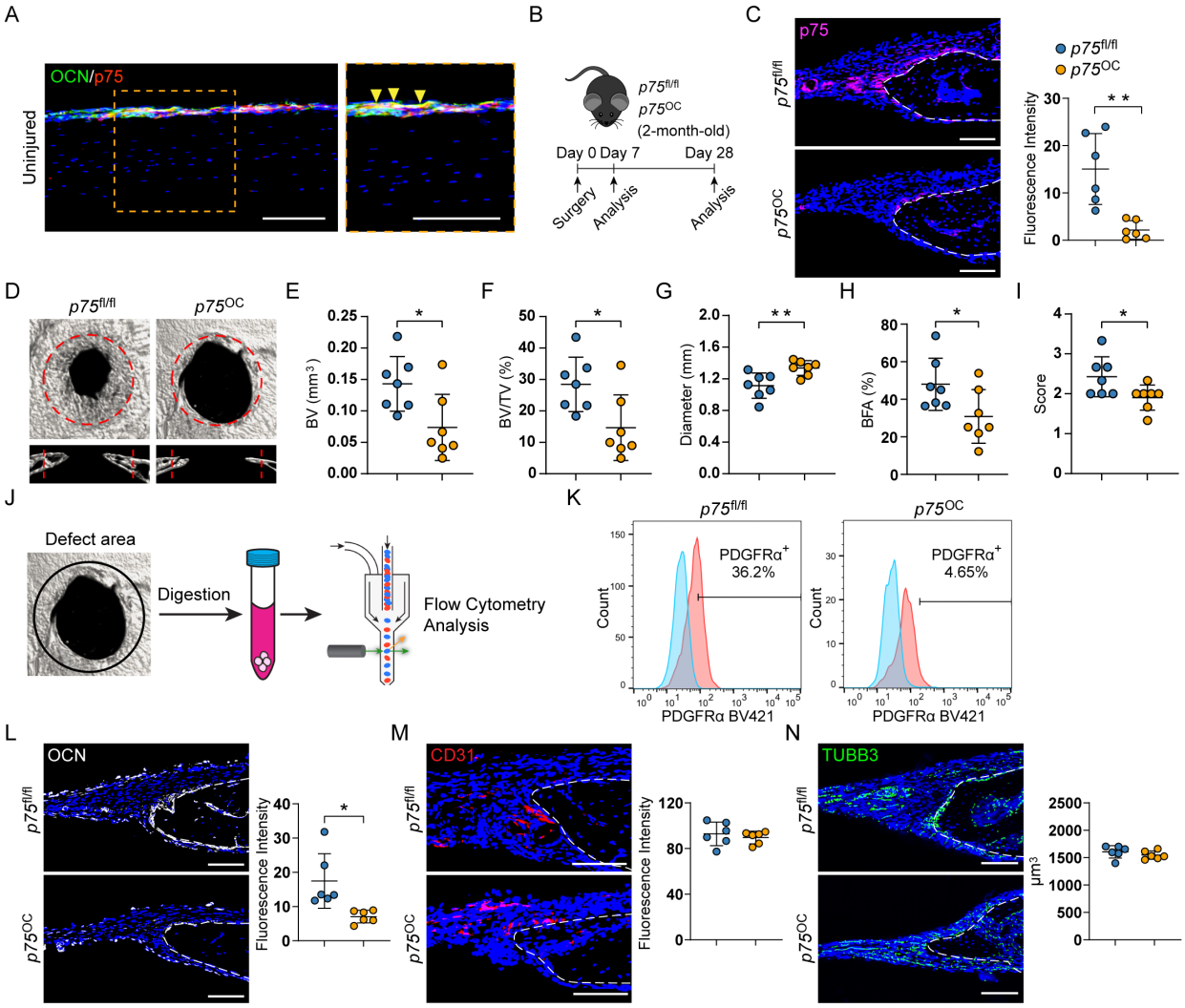

Fig. 2. Deletion of *p75* in Osteocalcin (OC)-expressing cells impairs osteoblast migration and calvarial defect healing. (A) Immunohistochemistry for p75 (red) and OCN (green) on the uninjured calvarial bone. Yellow arrowheads indicate p75 and OCN co-localization. **(B)** Schematic of experiment, in which $p75^{fl/fl}$ or $p75^{OC}$ animals (male, 2 mo old) were subjected to frontal bone injury (circular calvarial defect, 1.8 mm diameter), with analysis performed 7 or 28 d post-operatively. **(C)** Validation of *p75* deletion by p75 immunohistochemistry in either $p75^{fl/fl}$ or $p75^{OC}$ mice, d28 post-injury. White dashed lines indicate bone edges. **(D)** Micro-CT reconstructions of the defect site in a top down view (above) and coronal cross sectional images (below) among $p75^{fl/fl}$ and $p75^{OC}$ animals, 28 d post-injury. Margins of original defect are indicated by dashed red lines. **(E-I)** Micro-CT quantification of bone healing among $p75^{fl/fl}$ and $p75^{OC}$ mice (28 d post-injury), including **(E)** Bone volume (BV), **(F)** Bone volume/tissue volume (BV/TV), **(G)** residual defect diameter, **(H)** Bone formation area (BFA), and **(I)** Bone healing

715 score. **(J)** Schematic of experiment, in which calvarial defects from either *p75*$^{fl/fl}$ or *p75*^{OC}
716 animals were harvested at d7 post-injury, the original defect site was microdissected, tissue
717 dissociated and analyzed by flow cytometry. **(K)** Percentage of PDGFRα^{+} cells among freshly
718 isolated CD31^{-}CD45^{-}Ter119^{-} cells in the defect area from *p75*$^{fl/fl}$ or *p75*^{OC} animals. **(L-N)**
719 Immunohistochemical staining and semi-quantitative analysis of Osteocalcin (OCN) **(L)**, CD31
720 **(M)**, and Beta III Tubulin (TUBB3) **(N)** within the calvarial defect, 28 d post-injury. Dashed
721 white lines indicate bone edge. In graphs, each dot represents a single animal. White scale bar:
722 100 µm. N=3-4 mice per group for **(A,K)** and N=6-7 mice per group for **(C-I, L-N)**. Data are
723 represented as mean ± 1 SD. *P<0.05 and **P<0.01 as assessed using a two-tailed Student's *t*-
724 test.

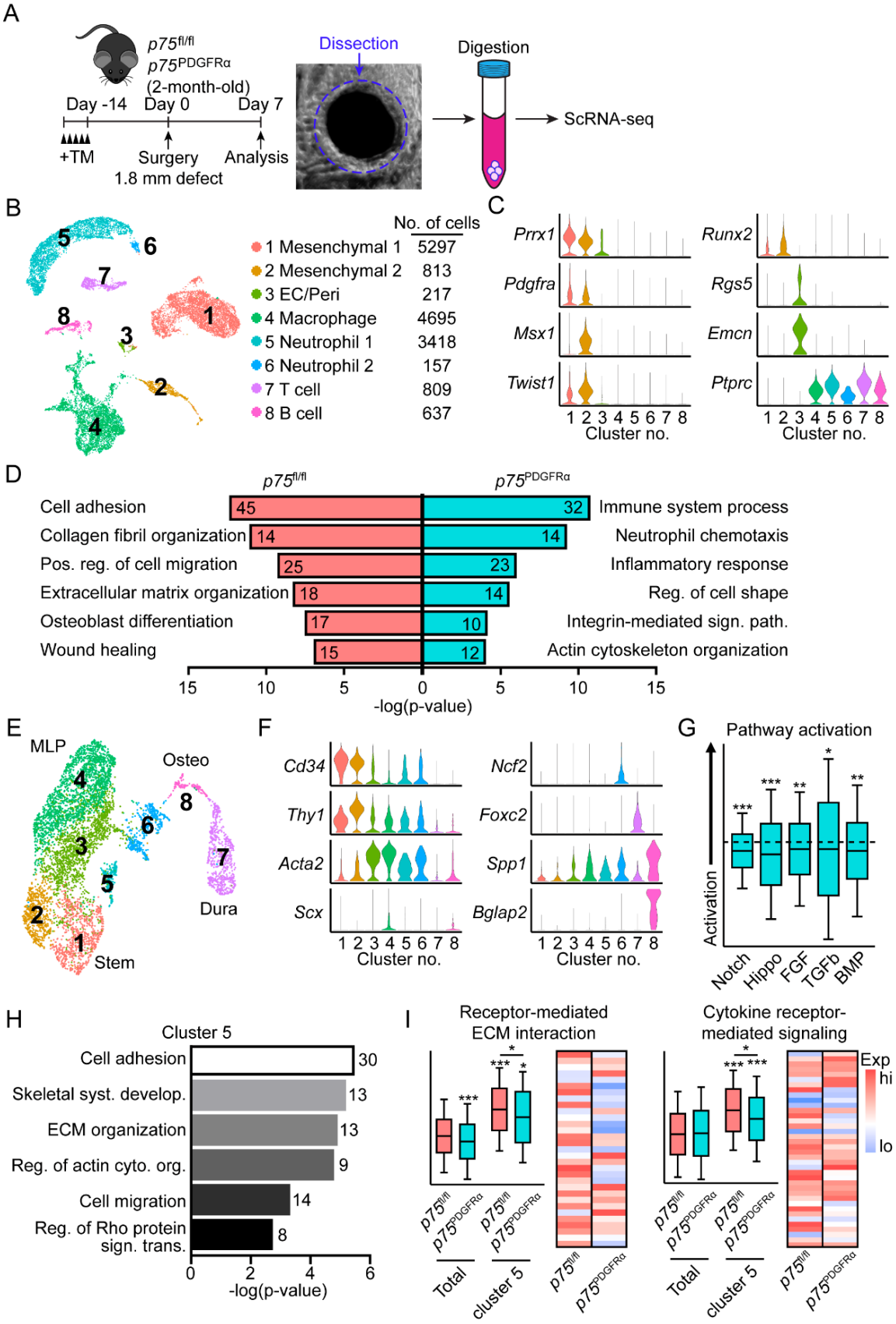
A
p75fl/fl
p75PDGFRα
(2-month-old)
Day -14
Day 0
Day 7
+TM
Surgery
Analysis
1.8 mm defect
Dissection
Digestion
ScRNA-seq
B
No. of cells
1 Mesenchymal 1 5297
2 Mesenchymal 2 813
3 EC/Peri 217
4 Macrophage 4695
5 Neutrophil 1 3418
6 Neutrophil 2 157
7 T cell 809
8 B cell 637
C
Prrx1
Pdgfra
Msx1
Twist1
Runx2
Rgs5
Emcn
Ptprc
Cluster no.
D
p75fl/fl
p75PDGFRα
Cell adhesion 45 32 Immune system process
Collagen fibril organization 14 14 Neutrophil chemotaxis
Pos. reg. of cell migration 25 23 Inflammatory response
Extracellular matrix organization 18 14 Reg. of cell shape
Osteoblast differentiation 17 10 Integrin-mediated sign. path.
Wound healing 15 12 Actin cytoskeleton organization
-log(p-value)
E
MLP
Osteo
Dura
Stem
F
Cd34
Thy1
Acta2
Scx
Ncf2
Foxc2
Spp1
Bglap2
Cluster no.
G
Pathway activation
Activation
Notch
Hippo
FGF
TGFb
BMP
H
Cluster 5
Cell adhesion 30
Skeletal syst. develop. 13
ECM organization 13
Reg. of actin cyto. org. 9
Cell migration 14
Reg. of Rho protein sign. trans. 8
-log(p-value)
I
Receptor-mediated ECM interaction
Cytokine receptor-mediated signaling
Total
cluster 5
Exp
hi
lo

725

726 **Fig. 3. Single cell transcriptomics highlights altered signaling pathway activation and**
727 **impaired cellular migration with *p75* conditional gene deletion. (A)** Schematic of experiment,
728 in which *p75*$^{fl/fl}$ or *p75*$^{PDGFR\alpha}$ animals (male, 2 mo old) were administered tamoxifen (TM),
729 subjected to frontal bone injury after 14 d (circular calvarial defect, 1.8 mm diameter), with
730 analysis performed 7 d post-operatively. The defect area was microdissected, dissociated and
731 subjected to single-cell RNA sequencing. **(B)** UMAP plot of total cells isolated from calvarial
732 defect site among *p75*$^{fl/fl}$ and *p75*$^{PDGFR\alpha}$ animals. EC: endothelial cell; Peri: pericyte. **(C)** Violin
733 plots of marker gene expression for mesenchymal, EC/Peri, and immune cell clusters. **(D)** GO
734 term analyses of enriched biological processes among all 16,043 cells from *p75*$^{fl/fl}$ and *p75*$^{Pdgfr\alpha}$
735 mice. **(E)** UMAP plot of mesenchymal and neuroectodermal cells only (clusters 1 and 2 in
736 subfigure B). MLP: Multilineage progenitor. **(F)** Violin plots of marker gene expression from
737 mesenchymal subclusters. **(G)** Specific pathway analysis among mesenchymal cells from
738 *p75*$^{Pdgfr\alpha}$ mice in comparison to *p75*$^{fl/fl}$ mice. **(H)** GO term analyses of enriched biological
739 processes among mesenchymal cluster 5. **(I)** Receptor-mediated ECM interaction and cytokine
740 receptor-mediated signaling among total mesenchymal clusters or cluster 5 from *p75*$^{fl/fl}$ and
741 *p75*$^{Pdgfr\alpha}$ mice. N=5 mice per group were used to yield a single cell population. **P*<0.05,
742 ***P*<0.01, and ****P*<0.001 as assessed using a Wilcoxon test or two-way ANOVA with Tukey's
743 multiple comparisons test.

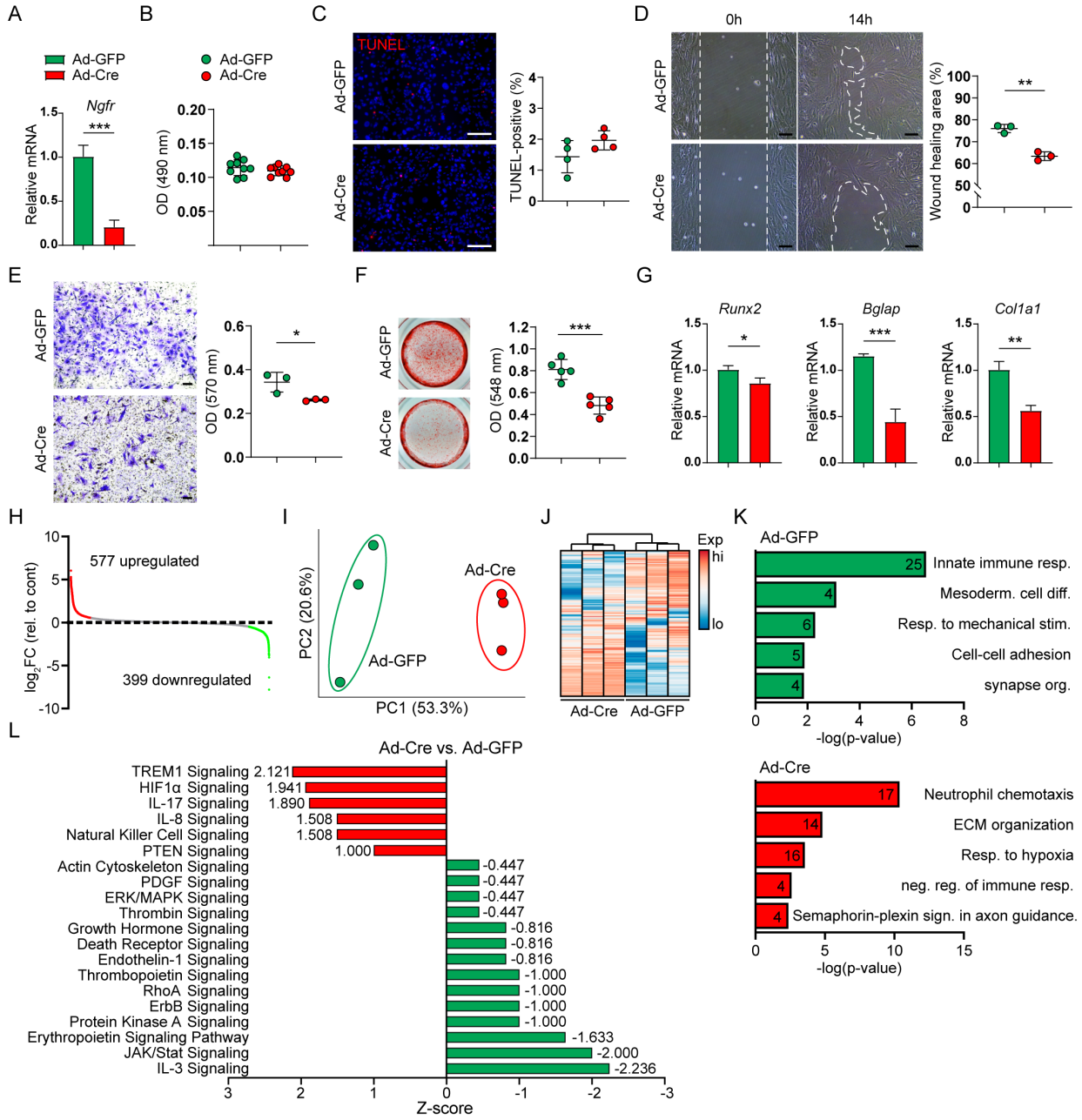

Fig. 4. Deletion of *p75* in NMCCs inhibits cell migration and mineralization. Neonatal mouse calvarial cells (NMCCs) were isolated from *p75*$^{fl/fl}$ mice and exposed to Adenoviral GFP (Ad-GFP) or Ad-Cre *in vitro*. **(A)** *Ngfr* expression by qRT-PCR among Ad-GFP- and Ad-Cre-treated cells after 72 hrs. **(B)** Cellular proliferation among Ad-GFP- and Ad-Cre-treated cells, by MTS assays at 72 h. **(C)** Apoptosis among Ad-GFP- and Ad-Cre-treated NMCCs by TUNEL assay. **(D,E)** Cellular migration assessed by **(D)** scratch wound healing assay at 14 h or **(E)** transwell assay at 4 h among Ad-GFP- and Ad-Cre-treated groups. Representative 100x images with percentage gap closure shown. **(F)** Osteogenic differentiation of Ad-GFP- and Ad-Cre-

753 treated NMCCs by Alizarin Red (AR) staining and quantification at 14 d. **(G)** Osteogenic gene
754 expression among Ad-GFP- and Ad-Cre-treated NMCCs, including *Runt-related transcription*
755 *factor 2* (*Runx2*), *Osteocalcin* (*Bglap*), and *Collagen type 1 a1* (*Col1a1*) at 7 d of differentiation.
756 **(H-L)** Bulk total RNA sequencing (Illumina NextSeq 500 platform) among Ad-GFP- and Ad-
757 Cre-treated NMCCs. **(H)** Differentially expressed genes (DEGs) of all 14,668 transcripts among
758 Ad-Cre-treated NMCCs. Y-axis represents Log2 fold change (FC) for each gene. The number of
759 upregulated DEGs (log2 FC ≥ 1, red dots) is 577, the number of downregulated DEGs (log2 fold
760 change ≤ −1, green dots) is 399. **(I)** Principal component analysis among Ad-GFP- and Ad-Cre-
761 treated cells. **(J)** Unsupervised hierarchical clustering among Ad-GFP- and Ad-Cre-treated
762 NMCCs. **(K)** DAVID functional GO analysis of biological processes enrichment among Ad-
763 GFP- and Ad-Cre-treated NMCCs. **(L)** QIAGEN Ingenuity Pathway Analysis (IPA) identified
764 representative pathways that were upregulated (Z-score > 0; red color) or downregulated (Z-
765 score < 0; green color) in Ad-Cre compared to Ad-GFP-treated NMCCs. Graphs represent mean
766 values, while error bars represent 1 SD. Dot plots represent an individual sample, while whisker
767 plots indicate mean values and 1 SD. *In vitro* experiments were performed in biologic and
768 experimental triplicate. Black scale bar: 100 μm. White scale bar: 10 μm. *P<0.05, **P<0.01,
769 and ***P<0.001 as assessed using a two-tailed Student's t-test.

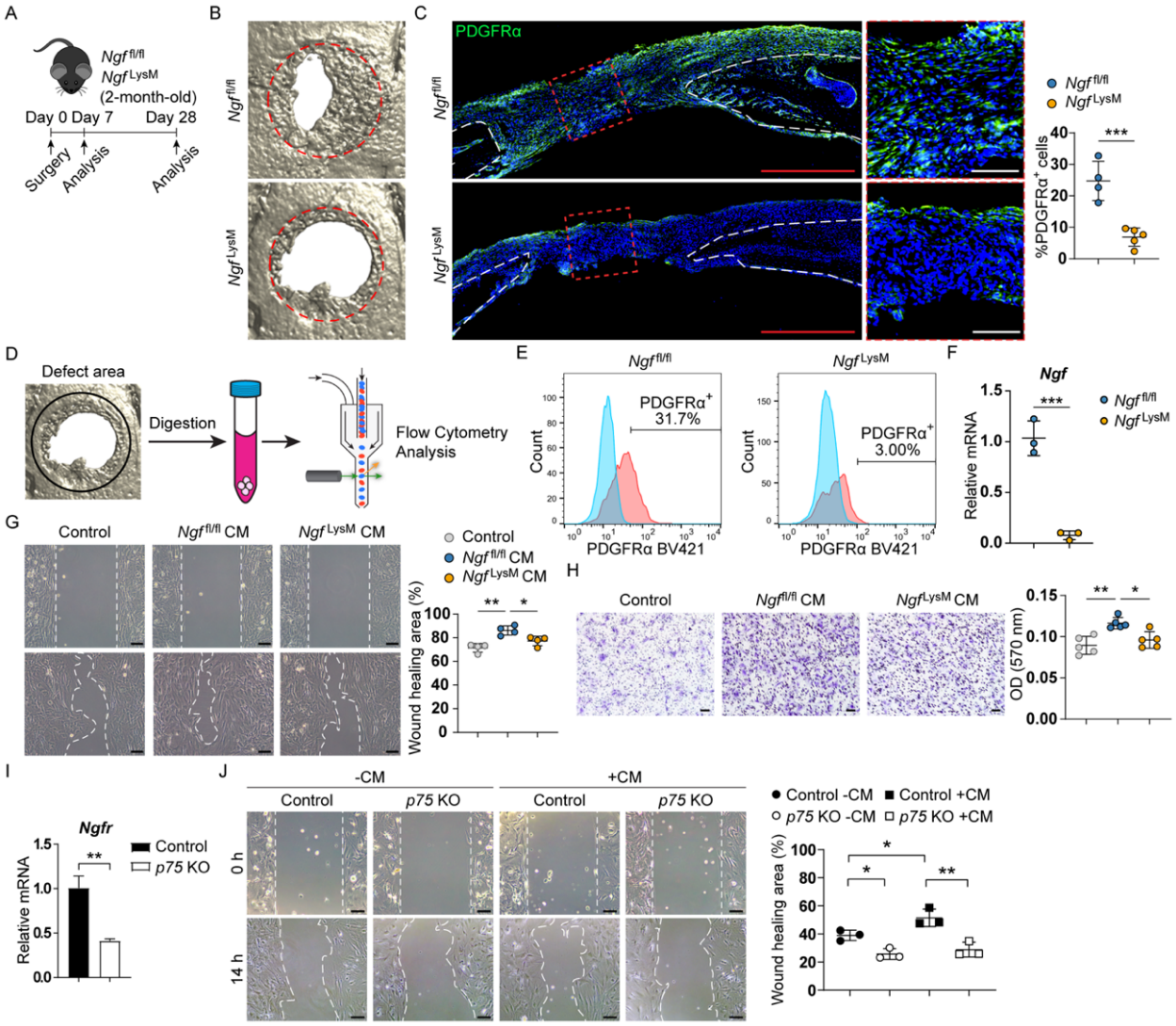

Fig. 5. Macrophage-derived NGF regulates NMCC migration by p75 signaling. (A) Schematic of experiment, in which *Ngf*$^{fl/fl}$ or *Ngf*^{LysM} animals (male, 2 mo old) were subjected to frontal bone injury (circular calvarial defect, 1.8 mm diameter), with analysis performed 7 or 28 d post-operatively. **(B)** Micro-CT reconstructions of the defect site in a top down view among *Ngf*$^{fl/fl}$ and *Ngf*^{LysM} animals. Margins of original defect are indicated by dashed red lines. **(C)** Stromal/osteoprogenitor cell migration among *Ngf*$^{fl/fl}$ and *Ngf*^{LysM} animals, as assessed by PDGFRα immunofluorescent staining. Tile scan (left) and high-magnification images of the defect site (right) demonstrate migration of PDGFRα^{+} progenitor cells into the defect site at d7 post-injury. White dashed lines indicate bone edges. **(D)** Schematic of experiment, in which calvarial from *Ngf*$^{fl/fl}$ or *Ngf*^{LysM} animals (male, 2 mo old) were harvested at d7 post-injury and only the defect area was left (black circle). After digestion, cells were incubated with antibodies

782 and analyzed by flow cytometry. **(E)** Percentage of PDGFRα^{+} cells among freshly isolated
783 CD31^{-}CD45^{-}Ter119^{-} cells in the defect area from *Ngf*$^{fl/fl}$ or *Ngf*^{LysM} animals. **(F)** Validation of
784 *Ngf* deletion in macrophages from *Ngf*^{LysM} mice in comparison to *Ngf*$^{fl/fl}$ mice. Quantitative RT-
785 PCR performed after isolation and expansion in M-CSF. **(G,H)** NMCC migration assessed by
786 **(G)** scratch wound healing assay at 14 h or **(H)** transwell assay at 4 h with normal medium
787 (Control) and conditional medium of cultured macrophages from *Ngf*$^{fl/fl}$ or *Ngf*^{LysM} mice.
788 Representative 100x images with percentage gap closure are shown. **(I)** Validation of *Ngfr*
789 deletion in NMCCs from *p75*^{PDGFRα} mice after 4-Hydroxytamoxifen treatment. **(J)** Migration of
790 NMCCs treated with or without 4-Hydroxytamoxifen assessed by scratch wound healing assay at
791 14 h with normal medium and conditional medium of cultured macrophages from *Ngf*$^{fl/fl}$ mice.
792 Representative 100x images with percentage gap closure are shown. Graphs represent mean
793 values, while error bars represent 1 SD. Dot plots represent an individual sample or animal,
794 while whisker plots indicate mean values and 1 SD. *In vitro* experiments were performed in
795 biologic and experimental triplicate **(F-J)**. Red scale bar: 500 µm. White scale bar: 100 µm.
796 N=4-5 per group for **(B-E)**. **P*<0.05, ***P*<0.01, and ****P*<0.001 as assessed using a two-tailed
797 Student's *t*-test or one-way ANOVA with Tukey's multiple comparisons test.

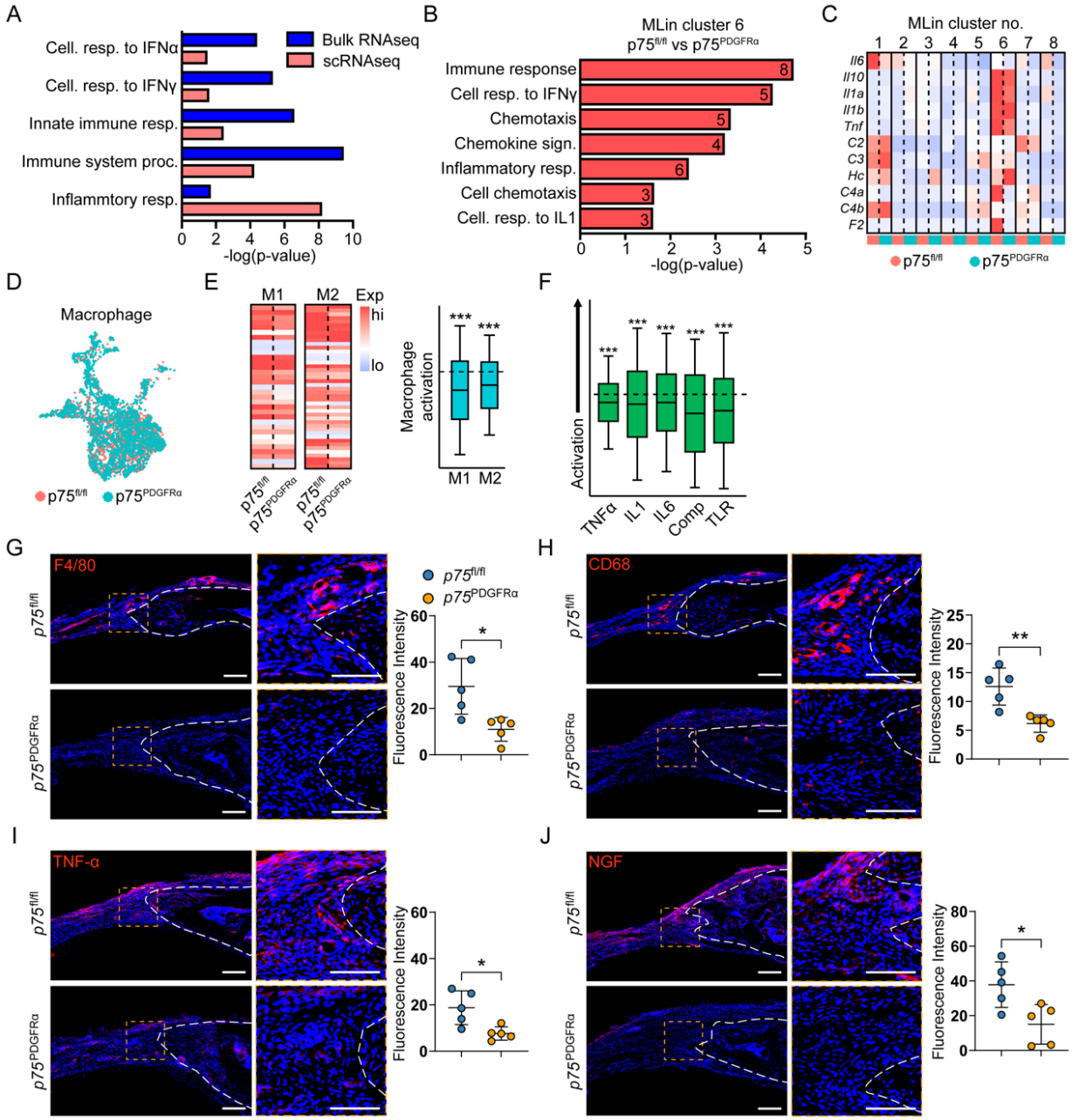

Fig. 6. Deletion of p75 in PDGFRa-expressing mesenchyme results in secondary inflammatory changes in the bone defect microenvironment. (A) GO term analyses of enriched biological processes among mesenchymal cluster 6. **(B)** The expression of inflammatory factors among mesenchymal clusters from *p75*$^{fl/fl}$ and *p75*$^{Pdgfr\alpha}$ mice. **(C)** Inflammatory pathways enriched in both NMCC bulk RNA-seq and mesenchymal clusters derived from scRNA-seq. **(D)** Distribution of macrophages from *p75*$^{fl/fl}$ and *p75*$^{Pdgfr\alpha}$ mice in UMAP plot. **(E)** Heat map of marker gene expression of M1 and M2 macrophages across *p75*$^{fl/fl}$

806 and *p75*$^{Pdgfr\alpha}$ mice (Left). The analysis of macrophage activation among *p75*$^{Pdgfr\alpha}$ mice in
807 comparison to *p75*$^{fl/fl}$ mice. (Right). Dashed black line indicates the same activity of macrophage
808 polarization across *p75*$^{fl/fl}$ and *p75*$^{Pdgfr\alpha}$ genotypes. **(F)** The expression of inflammatory factors
809 among macrophages from *p75*$^{Pdgfr\alpha}$ mice in comparison to *p75*$^{fl/fl}$ mice. Dashed black line
810 indicates the same expression of inflammatory factors across *p75*$^{fl/fl}$ and *p75*$^{Pdgfr\alpha}$ genotypes. **(G-**
811 **J)** Immunohistochemical staining and semi-quantitative analysis of F4/80 **(G)**, CD68 **(H)**, Tumor
812 Necrosis Factor (TNF)-α **(I)**, and Nerve Growth Factor (NGF) **(J)** within the calvarial defect, d7
813 post-injury. Dashed white lines indicate bone edges. In graphs, each dot represents a single
814 animal. White scale bar: 100 μm. N=5 mice per group for **(G-J)**. Data are represented as mean ±
815 1 SD. **P*<0.05, ***P*<0.01, and ****P*<0.001 as assessed using a Wilcoxon test or two-tailed
816 Student's *t*-test.

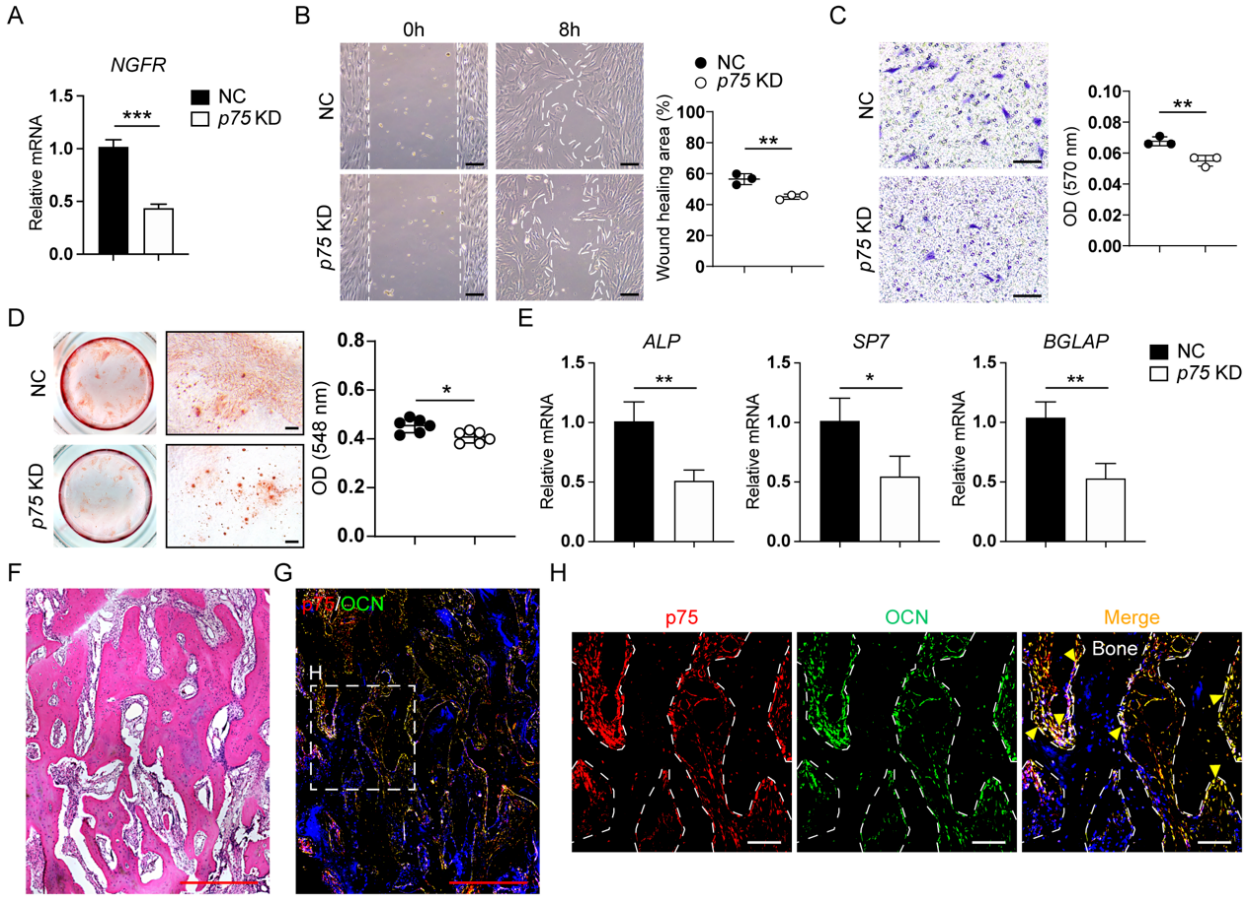

Fig. 7. Deletion of *p75* in human calvarial osteoblasts inhibits cell migration and mineralization. (A) *NGFR* expression by qRT-PCR after siRNA-mediated knockdown in human calvarial osteoblasts. NC, negative control (non-targeting siRNA). **(B,C)** Cellular migration assessed by **(B)** scratch wound healing assay at 8 h or **(C)** transwell assay at 4 h with or without *p75* siRNA. Representative 100x images with percentage gap closure shown. **(D)** Osteogenic differentiation after siRNA-mediated knockdown in human calvarial osteoblasts by Alizarin Red (AR) staining and quantification at 7 d. **(E)** Osteogenic gene expression with or without *p75* siRNA, including *Alkaline phosphatase* (*ALP*), *Osterix* (*SP7*), and *Osteocalcin* (*BGLAP*) at 7 d of differentiation. **(F)** Representative histologic appearance of a healing human fracture by H&E staining. **(G)** Immunohistochemistry for p75 (red) and Osteocalcin (OCN, green) in healing human fracture sites (N=3). Nuclei, DAPI (blue). Dashed box indicates the location of H. **(H)** High magnification image for p75 (red) and OCN (green) expression in the bone lining osteoblasts. Yellow arrowheads indicate p75 and OCN co-localization. White dashed lines indicate bone edges. Graphs represent mean values, while error bars represent 1 SD. Dot

plots represent an individual sample, while whisker plots indicate mean values and 1 SD. *In vitro* experiments were performed in biologic and experimental triplicate. Red scale bar: 500 μm. Black/white scale bar: 100 μm. *$P<0.05$, **$P<0.01$, and ***$P<0.001$ as assessed using a two-tailed Student's *t*-test.